FILTERED KIRCHHOFF MIGRATION OF CROSS CORRELATIONS OF AMBIENT NOISE SIGNALS

JOSSELIN GARNIER* AND KNUT SØLNA[†]

Abstract. In this paper we study passive sensor imaging with ambient noise sources by suitably migrating cross correlations of the recorded signals. We propose and study different imaging functionals. A new functional is introduced that is an inverse Radon transform applied to a special function of the cross correlation matrix. We analyze the properties of the new imaging functional in the high-frequency regime which shows that it produces sharper images than the usual Kirchhoff migration functional. Numerical simulations confirm the theoretical predictions.

Key words. Passive sensor imaging, noise sources, cross correlation.

AMS subject classifications. 35R30, 35R60, 86A15.

1. Introduction. Estimation of the Green's function of the wave equation in an inhomogeneous medium by cross correlation of noisy signals has recently attracted a lot of attention. Consider the situation in which noise sources with unknown spatial support emit stationary random signals, that propagate into the medium and are recorded at observation points. The cross correlation of the recorded signals has then been shown to provide a reliable estimate of the Green's function and the travel time between the observation points [14, 16, 20]. The mathematical analysis of cross correlation of noisy signals was carried out in [9, 11, 12, 13]. The travel time estimates can then be used for background velocity estimation [10, 18]. Tomographic travel time velocity analysis, based on cross correlations, was applied successfully for surface-wave velocity estimation in Southern California [17], in Tibet [21], and in the Alps [19].

Cross correlations of noisy signals recorded by a passive sensor array can also be processed in order to image the medium. The idea presented in [13] is to backpropagate the cross correlation matrix by applying a simple Kirchhoff migration (KM) functional, which is a technique widely used in active seismic imaging [3, 8]. The images are qualitatively good with cross range and range resolutions equivalent to those that would be obtained by migrating the impulse response matrix obtained with an active sensor array. However, direct backpropagation of the data set is known to be sub-optimal in the context of active array imaging and improved imaging functionals based on High-Frequency Inversion (HFI) have been obtained in this context [2, 4]. Our goal in this paper is to present an efficient imaging functional in the context of passive array imaging.

In this paper we assume a typical configuration in geophysics in which the passive sensor array is at the surface of the half-space to be imaged. We consider the situation in which the medium is two-dimensional. We analyze both the problem of the localization of the noise sources (Section 3) and the problem of the localization of scatterers embedded in the medium (Section 4) using the cross correlation matrix of the recorded signals. We propose an imaging functional that is an inverse Radon transform applied to a function of the cross correlation matrix. This function is obtained by summing the cross correlations evaluated at some special travel times over a limited offset range. By a high-frequency asymptotic analysis and by numerical

*Laboratoire de Probabilités et Modèles Aléatoires & Laboratoire Jacques-Louis Lions, Université Paris VII, 2 Place Jussieu, 75251 Paris Cedex 5, France `garnier@math.jussieu.fr`

[†]Mathematics Department, University of California at Irvine, Irvine, CA 92697 `ksolna@math.uci.edu`

simulations we will show that this new imaging functional produces sharper images than the usual KM or HFI functionals.

2. Empirical and statistical cross correlations. We consider the solution u of the wave equation in a *two-dimensional* inhomogeneous medium with background velocity $c(\boldsymbol{x})$:

$$\frac{1}{c^2(\boldsymbol{x})} \frac{\partial^2 u}{\partial t^2} - \Delta_{\boldsymbol{x}} u = n(t, \boldsymbol{x}), \tag{2.1}$$

with $\boldsymbol{x} = (x, z)$. The source term $n(t, \boldsymbol{x})$ models a random distribution of noise sources and is supported in the halfspace $z < 0$. It is assumed to be a stationary process in time. For the sake of simplicity, we will assume that it has Gaussian statistics and that it is delta-correlated in space, so that its autocorrelation function has the form

$$\langle n(t_1, \boldsymbol{y}_1) n(t_2, \boldsymbol{y}_2) \rangle = F(t_2 - t_1) K(\boldsymbol{y}_1) \delta(\boldsymbol{y}_1 - \boldsymbol{y}_2). \tag{2.2}$$

Here the brackets stand for the statistical averaging with respect to the distribution of the sources. The Fourier transform of the autocorrelation function $F(t)$:

$$\hat{F}(\omega) = \int F(t) e^{i\omega t} dt$$

is proportional to the power spectral density of the signals emitted by the noise sources. The function $\hat{F}(\omega)$ is nonnegative valued and we assume that its support is bounded away from zero and from infinity. Note that this function is not known so that we look for imaging procedures that are robust with respect to its form. The function $K(\boldsymbol{y})$ is supposed to be compactly supported and its support characterizes the source region. It is possible to carry out the analysis with more complex models, such as the one described in [1], but this would not change the main points of the paper.

The empirical cross correlation of the signals recorded at two points $\boldsymbol{x}_1$ and $\boldsymbol{x}_2$ is defined by:

$$C_T(\tau, \boldsymbol{x}_1, \boldsymbol{x}_2) = \frac{1}{T} \int_0^T u(t, \boldsymbol{x}_1) u(t + \tau, \boldsymbol{x}_2) dt. \tag{2.3}$$

As shown in [13], it is a statistically stable quantity in the sense that it converges to its statistical mean when the integration time T goes to infinity:

$$C_T(\tau, \boldsymbol{x}_1, \boldsymbol{x}_2) \stackrel{T \to \infty}{\longrightarrow} C(\tau, \boldsymbol{x}_1, \boldsymbol{x}_2),$$

where $C(\tau, \boldsymbol{x}_1, \boldsymbol{x}_2)$ is the statistical cross correlation defined by

$$C(\tau, \boldsymbol{x}_1, \boldsymbol{x}_2) = \langle C_T(\tau, \boldsymbol{x}_1, \boldsymbol{x}_2) \rangle = \langle u(0, \boldsymbol{x}_1) u(\tau, \boldsymbol{x}_2) \rangle. \tag{2.4}$$

Writing the recorded field in terms of the Green's function and the source term, and using the particular form of the autocorrelation function of the sources, we obtain the expression:

$$C(\tau, \boldsymbol{x}_1, \boldsymbol{x}_2) = \frac{1}{2\pi} \iint \overline{\hat{G}}(\omega, \boldsymbol{x}_1, \boldsymbol{y}) \hat{G}(\omega, \boldsymbol{x}_2, \boldsymbol{y}) e^{-i\omega\tau} \hat{F}(\omega) K(\boldsymbol{y}) d\boldsymbol{y} d\omega, \tag{2.5}$$

where $\hat{G}$ is the outgoing time-harmonic Green's function. When the background velocity is homogeneous $c(\boldsymbol{x}) = c_0$, the Green's function is given by

$$\hat{G}(\omega, \boldsymbol{x}, \boldsymbol{y}) = \frac{i\,\mathrm{sgn}(\omega)}{4} H_0^{(1)}\left(\frac{\omega}{c_0}|\boldsymbol{y} - \boldsymbol{x}|\right), \tag{2.6}$$

where $H_0^{(1)}$ is the zeroth order Hankel function of the first kind. Using the asymptotic form of the Hankel function $H_0^{(1)}(x) \simeq \sqrt{2/(\pi|x|)}\exp[ix - i\,\mathrm{sgn}(x)\pi/4]$ for $|x| \gg 1$, we find that for $|\omega||\boldsymbol{x} - \boldsymbol{y}|/c_0 \gg 1$:

$$\hat{G}(\omega, \boldsymbol{x}, \boldsymbol{y}) = \frac{\sqrt{c_0}}{2\sqrt{2\pi}}\frac{e^{i\,\mathrm{sgn}(\omega)\pi/4}}{\sqrt{|\omega||\boldsymbol{y} - \boldsymbol{x}|}}\exp\left(i\frac{\omega}{c_0}|\boldsymbol{y} - \boldsymbol{x}|\right). \tag{2.7}$$

We remark that more generally in this regime the Green's function can be approximated by the geometrical optics or WKB approximation

$$\hat{G}(\omega, \boldsymbol{x}, \boldsymbol{y}) = A(\boldsymbol{x}, \boldsymbol{y}, \omega)e^{i\omega\tau(\boldsymbol{x}, \boldsymbol{y})},$$

with A and τ being the geometrical optics amplitude and travel time (in between $\boldsymbol{x}$ and $\boldsymbol{y}$) that solve respectively transport and Eiconal equations. We shall here focus on the case with constant background.

3. Imaging the source distribution. We consider an array of N passive sensors located at the surface $z = 0$ at $(\boldsymbol{x}_j)_{j=1,\ldots,N}$, with $\boldsymbol{x}_j = (x_j, 0)$, $x_j \in \mathbb{R}$. The data set consists of the empirical cross correlation matrix $(C_T(\tau, \boldsymbol{x}_j, \boldsymbol{x}_l))_{j,l=1,\ldots,N}$. We want to process this data set to build an imaging functional for the source locations.

3.1. High-frequency analysis. We will propose an imaging functional based on the analysis of the statistical cross correlation in the continuum approximation $(C(\tau, x_1, x_2))_{x_1, x_2 \in \mathbb{R}}$. Here $C(\tau, x_1, x_2)$ is a shorthand for $C(\tau, (x_1, 0), (x_2, 0))$.

We introduce the coherence time τ_c of the sources, which is the width of the autocorrelation function F. We say that we are in the high-frequency regime if τ_c is much smaller than the typical travel time τ_0 between the sources and the sensors. Thus, we make

ASSUMPTION 1. $\tau_c \ll \tau_0$.

In the high-frequency regime, we can use the high-frequency (or geometric optics) approximation (2.7) of the Green's function and we find that the cross correlation function has the form

$$C(\tau, x_1, x_2) = \frac{1}{2\pi}\int \hat{C}(\omega, x_1, x_2)e^{-i\omega\tau}d\omega, \tag{3.1}$$

$$\hat{C}(\omega, x_1, x_2) = \frac{\hat{F}(\omega)}{|\omega|}\int K(\boldsymbol{y})a\big((x_1, 0), \boldsymbol{y}\big)a\big((x_2, 0), \boldsymbol{y}\big)e^{i\omega[\tau((x_2,0),\boldsymbol{y})-\tau((x_1,0),\boldsymbol{y})]}d\boldsymbol{y}, \tag{3.2}$$

where

$$a(\boldsymbol{x}, \boldsymbol{y}) = \frac{\sqrt{c_0}}{2\sqrt{2\pi}\sqrt{|\boldsymbol{x} - \boldsymbol{y}|}} \text{ and } \tau(\boldsymbol{x}, \boldsymbol{y}) = \frac{|\boldsymbol{x} - \boldsymbol{y}|}{c_0}.$$

At this point, a typical strategy would be to backpropagate the data set, which is the cross correlation matrix in our context. This means that, for the search point $\boldsymbol{y}^S$, one would look for an imaging functional of the form

$$\mathcal{I}(\boldsymbol{y}^S) = \iint \hat{B}(\omega, \boldsymbol{y}^S, x_1, x_2)e^{i\omega[\tau((x_1,0),\boldsymbol{y}^S)-\tau((x_2,0),\boldsymbol{y}^S)]}\hat{C}(\omega, x_1, x_2)d\omega dx_1 dx_2, \tag{3.3}$$

where the kernel $\hat{B}$ is to be determined so that $\mathcal{I}(\boldsymbol{y}^S)$ is as close as possible to $K(\boldsymbol{y}^S)$ [2, 4] when the objective is to image the source distribution. We will show in the following that it is possible to write the expression of the cross correlation matrix in such a way that an efficient imaging formula can be obtained simply in terms of an *inverse Radon transform.*

Up front we would like to stress two differences in our formulation relative to the one in a classic seismic imaging situation with standard seismic reflection data. First, the difference in travel times appears in the phase term of the high-frequency expression of the cross correlation (3.2) instead of the sum. Second, the cross correlation function has both causal and anti-causal contributions [13].

We will now introduce the central functional of the cross correlations that will be convenient for localizing scatterers and noise sources and describe next how this functional in fact gives a Radon transform of the data. Let us consider for $s \in \mathbb{R}$ and $\phi \in (-\pi/2, \pi/2)$ the function

$$R(s, \phi) = \cos \phi \int_{-\infty}^{\infty} C\Big(\frac{\sin \phi}{c_0} y, \frac{s}{\cos \phi} + \frac{y}{2}, \frac{s}{\cos \phi} - \frac{y}{2}\Big) dy. \qquad (3.4)$$

In this integral function we sum the cross correlation over all pairs of surface sensors with fixed midpoint $s/\cos \phi$ over all interstation offsets y and associated time delays $y \sin \phi / c_0$. This time delay corresponds to the delay observed between the signals recorded at the two sensors for a signal emitted by a point source located in the far field in the direction ϕ with respect to the vertical direction and a distance s from the origin. Thus, this functional gives directional and support information about the incoming wave field generated by the sources.

A key observation is now that the function R is essentially the Radon transform of the source distribution K. In fact, the function R is related to the source distribution function K is the following way:

PROPOSITION 3.1. *In the high-frequency regime the function R is proportional to the Radon transform of K:*

$$R(s, \phi) \simeq r_0 \, \mathrm{RT}\big(K\big)(s, \phi), \qquad (3.5)$$

$$\mathrm{RT}\big(K\big)(s, \phi) = \int K\big(s \cos \phi - u \sin \phi, s \sin \phi + u \cos \phi\big) du, \qquad (3.6)$$

where r_0 is the constant defined by:

$$r_0 = \frac{c_0}{8\pi} \int \frac{\hat{F}(\omega)}{\omega^2} d\omega. \qquad (3.7)$$

This proposition shows that the application of the inverse Radon transform to the function R gives the function K, which provides the principle for the imaging method introduced in the next subsection.

Proof. We first consider for $x \in \mathbb{R}$ and $\alpha \in (-1, 1)$ the function

$$W_s(x, \alpha) = \frac{1 - \alpha^2}{c_0} \int C\Big(\frac{\alpha}{c_0} y, x + \frac{y}{2}, x - \frac{y}{2}\Big) dy. \qquad (3.8)$$

The function W_s can also be seen as the frequency-averaged Wigner transform of the

cross correlation:

$$W_s(x, \alpha) = \frac{1 - \alpha^2}{2\pi c_0} \int W(\omega, x, \alpha) d\omega,$$

$$W(\omega, x, \alpha) = \iint C\left(\tau, x + \frac{y}{2}, x - \frac{y}{2}\right) \exp\left(-i\frac{\omega}{c_0}\alpha y + i\omega\tau\right) d\tau dy.$$

In the high-frequency regime, we can use the high-frequency approximation of the Green's function. Substituting (3.1-3.2) into (3.8), we find that in the high-frequency regime W_s is equal to

$$W_s(x, \alpha) = \frac{1 - \alpha^2}{16\pi^2} \iint \frac{K(x_s, z_s)}{\sqrt{z_s^2 + (x_s - x)^2}} \frac{\hat{F}(\omega)}{|\omega|}$$
$$\times \exp\left(-i\frac{\omega}{c_0}\left[\alpha + \frac{x - x_s}{\sqrt{z_s^2 + (x - x_s)^2}}\right]y\right) dydz_sdx_sd\omega.$$

Integrating in y gives a Dirac distribution:

$$W_s(x, \alpha) = \frac{c_0(1 - \alpha^2)}{8\pi} \iint \frac{K(x_s, z_s)}{\sqrt{z_s^2 + (x_s - x)^2}} \frac{\hat{F}(\omega)}{\omega^2} \delta\left(\alpha + \frac{x - x_s}{\sqrt{z_s^2 + (x - x_s)^2}}\right) dz_sdx_sd\omega.$$

Denoting $f(x_s) = \alpha + (x - x_s)/\sqrt{z_s^2 + (x - x_s)^2}$, there is a unique point X_s such that $f(X_s) = 0$:

$$X_s = x - z_s\frac{\alpha}{\sqrt{1 - \alpha^2}},$$

and we have the identity between distributions:

$$\delta\big(f(x_s)\big) = \frac{1}{\left|\frac{df}{dx_s}(X_s)\right|}\delta\big(x_s - X_s\big).$$

We then find

$$W_s(x, \alpha) = r_0 \int K\left(x - \frac{\alpha}{\sqrt{1 - \alpha^2}}z_s, z_s\right) dz_s, \tag{3.9}$$

with r_0 given by (3.7).

The function R defined by (3.4) can be expressed as

$$R(s, \phi) = W_s\left(\frac{s}{\cos\phi}, \sin\phi\right)\frac{c_0}{\cos\phi}, \quad (s, \phi) \in \mathbb{R} \times (-\pi/2, \pi/2). \tag{3.10}$$

Therefore, in the high-frequency regime we have (3.5), which is the standard form of the Radon transform. □

By looking at a transformation of the cross correlation, it is also possible to get the following result.

COROLLARY 3.2. *Let us consider for $s \in \mathbb{R}$ and $\phi \in (-\pi/2, \pi/2)$ the function*

$$R^{(h)}(s, \phi) = -\cos\phi \int_{-\infty}^{\infty} \partial_\tau^2 C\left(\frac{\sin\phi}{c_0}y, \frac{s}{\cos\phi} + \frac{y}{2}, \frac{s}{\cos\phi} - \frac{y}{2}\right) dy, \tag{3.11}$$

In the high-frequency regime the function $R^{(h)}$ is proportional to the Radon transform of K:

$$R^{(h)}(s, \phi) \simeq r_0^{(h)} \, \mathrm{RT}\big(K\big)(s, \phi), \tag{3.12}$$

where $r_0^{(h)}$ is proportional to the energy released by the sources:

$$r_0^{(h)} = \frac{c_0}{8\pi} \int \hat{F}(\omega) d\omega. \tag{3.13}$$

Note that this result involves the second τ-derivative of the cross correlation, which is usually less stable than the cross correlation itself. That is why we will propose an imaging functional based on the formulation of Proposition 3.1.

3.2. Imaging functional. From the empirical cross correlations we evaluate

$$R_T(s, \phi) = \cos\phi \int_{-\infty}^{\infty} C_T\left(\frac{\sin\phi}{c_0}y, \frac{s}{\cos\phi} + \frac{y}{2}, \frac{s}{\cos\phi} - \frac{y}{2}\right) dy. \tag{3.14}$$

In practice, the empirical cross correlation $C_T(\tau, x, y)$ is known only for x, y corresponding to sensor locations. Therefore, in order to evaluate $R_T(s, \phi)$ for a given pair (s, ϕ) it is necessary to use a quadrature formula whose points correspond to the sensor locations. In the numerical applications we use a Riemann sum based on a linear interpolation formula.

The Filtered Kirchhoff Migration (FKM) imaging functional is obtained by applying the Inverse Radon transform (IRT) to the empirical function R_T:

$$\mathcal{I}^{\text{FKM}}\big((x, z)\big) = \text{IRT}\big(R_T\big)(x, z). \tag{3.15}$$

We recall the principle of the IRT [15] in two dimensions:

$$R_T(s, \phi) \xrightarrow{\text{FT}(s \to \xi)} \hat{R}_T(\xi, \phi) \xrightarrow{\times |\xi|} |\xi| \hat{R}_T(\xi, \phi) \xrightarrow{\text{IFT}(\xi \to s)} \tilde{R}_T(s, \phi) \xrightarrow{\text{BP}} \text{IRT}(R_T)(x, z),$$

where FT (resp., IFT) is the direct (resp., inverse) Fourier transform and the final backpropagation (BP) step is

$$\text{IRT}\big(R_T\big)(x, z) = \int_{-\pi/2}^{\pi/2} \tilde{R}_T\big(x\cos\phi + z\sin\phi, \phi\big) d\phi.$$

In practice we use a Riemann sum approximation for the backpropagation step and FFTs for the Fourier transforms.

The backpropagation step is natural: it consists in summing up the Radon projections along all angles passing through the same point (x, z):

$$\mathcal{I}^{\text{BP}}\big((x, z)\big) = \int_{-\pi/2}^{\pi/2} R_T\big(x\cos\phi + z\sin\phi, \phi\big) d\phi. \tag{3.16}$$

As mentioned above a Riemann sum approximation is used to evaluate the integral in practice. However, the backpropagation alone gives a blurred recovery, and it is important to apply the inverse filter in order to fully recover the original function.

In practice, it can be useful to truncate the evaluation of the function R_T to a limited offset range $y \in (-y_{\max}, y_{\max})$:

$$R_T(s, \phi) = \cos\phi \int_{-y_{\max}}^{y_{\max}} C_T\left(\frac{\sin\phi}{c_0}y, \frac{s}{\cos\phi} + \frac{y}{2}, \frac{s}{\cos\phi} - \frac{y}{2}\right) dy. \tag{3.17}$$

There are two reasons that motivate this truncation:

1) Contributions of cross correlations with large offsets y to R_T may not bring any new coherent information, but only noise. This happens when the medium is cluttered, so that the signals recorded at two far points are not correlated anymore, or when the background velocity is not known exactly, this results in a significant error for the travel time quantity $y \sin \phi / c_0$ for large y. The choice of the parameter $y_{\max}$ results from a trade off between loss of resolution and noise reduction: When choosing a small $y_{\max}$, the noise level can be reduced, but the resolution can be reduced as well. Such a phenomenon was studied in the context of coherent interferometric imaging (CINT) for active array imaging [5, 6] and in the context of passive sensor imaging with cross correlations in a scattering medium [13].

2) A second reason why we should truncate the evaluation of the function R_T to a limited offset range is that for large offset y, the difference in travel times is more complicated than a linear function in y and this induces slight distortions in the image when we apply the IRT to R_T. In the limit $\tau_c / \tau_0 \to 0$ this distortion vanishes, which is the result of the high-frequency analysis. However such distortions can appear in practice when τ_c / τ_0 is not very small.

Finally, in practice, it is important to use a regularized inverse filter in order to have a stable inverse Radon transform algorithm and suppress noise. This means that we do not apply a multiplication by $|\xi|$ to the Fourier transform $\hat{R}_T(\xi, \phi)$ because it may amplify high-frequency noise. Instead, we apply a multiplication by a function of the form $|\xi| A(\xi)$, where A is an apodizing function that goes to zero as $|\xi| \to \infty$. The optimal choice of the apodizing function is subject to considerable work and it results from a trade-off between resolution and noise reduction. For instance $A(\xi) = \mathrm{sinc}^3(d\xi/2)$ for the Shepp-Logan filter [15]. In this case the resolution is limited to d.

3.3. Comparison with Kirchhoff migration. Kirchhoff migration (KM) consists in backpropagating the cross correlations using the known background travel times. It was studied in [13]. The KM imaging functional at a search point $\boldsymbol{y}^S$ is

$$\mathcal{I}^{\mathrm{KM}}(\boldsymbol{y}^S) = \sum_{j,l=1}^{N} C_T\big(\tau(\boldsymbol{y}^S, \boldsymbol{x}_l) - \tau(\boldsymbol{y}^S, \boldsymbol{x}_j), \boldsymbol{x}_j, \boldsymbol{x}_l\big). \qquad (3.18)$$

In the frequency domain, this means that a matched filter is applied in order to compensate for the phase term in the high-frequency expression of the cross correlation (3.2).

In this subsection we compare the KM and FKM functionals in the high-frequency regime.

The KM imaging functional in the continuum approximation is given by

$$\mathcal{I}^{\mathrm{KM}}\big((x,z)\big) = \iint C\Big(\frac{1}{c_0}\big[\sqrt{z^2 + (x-x_2)^2} - \sqrt{z^2 + (x-x_1)^2}\big], x_1, x_2\Big) dx_1 dx_2 . \qquad (3.19)$$

We then find that, in the high-frequency regime:

$$\mathcal{I}^{\mathrm{KM}}\big((x,z)\big) = \int_{-\infty}^{\infty} \int_{-\pi/2}^{\pi/2} C\Big(\frac{\sin\phi}{c_0}y', x + z\tan\phi + \frac{y'}{2}, x + z\tan\phi - \frac{y'}{2}\Big) \frac{|z|}{\cos^2\phi} d\phi dy'$$

$$= c_0 r_0 \iint K\Big(x + y_s\big(1 - \frac{z}{z_s}\big), z_s\Big) \frac{|z|(y_s^2 + z_s^2)}{|z_s|^3} dy_s dz_s, \qquad (3.20)$$

where r_0 is the constant given by (3.7). Note that, if K is localized around some point (x_0, z_0), then the integral in z_s is concentrated at z_0, and the integral over y_s

is stationary if and only if $z \simeq z_0$ and $x \simeq x_0$. That is why this imaging functional gives a reasonable image, although it is not perfect.

If we apply the BP functional (3.16) to the cross correlation in the continuum approximation (which amounts to apply the IRT without filtering), then we get in the continuum approximation and in the high-frequency regime:

$$
\mathcal{I}^{\mathrm{BP}}\big((x,z)\big) = \int_{-\infty}^{\infty} \int_{-\pi/2}^{\pi/2} C\Big(\frac{\sin\phi}{c_0}y', x + z\tan\phi + \frac{y'}{2}, x + z\tan\phi - \frac{y'}{2}\Big) \cos\phi \, d\phi \, dy'
$$

$$
= c_0 r_0 \iint K\Big(x + y_s\big(1 - \frac{z}{z_s}\big), z_s\Big) \frac{1}{\sqrt{z_s^2 + y_s^2}} dy_s \, dz_s, \qquad (3.21)
$$

which is equal to (3.20) up to an amplitude factor in the integral.

Therefore, the KM functional is very close to the BP functional. Since the IRT is known to perform better than BP in terms of resolution [15], we can claim that the functional $\mathcal{I}^{\mathrm{FKM}}$ is more efficient than the functional $\mathcal{I}^{\mathrm{KM}}$, with a computational cost that is almost equivalent ($N^2 \log N$ instead of N^2 for each search point or for each pixel of the reconstruction grid).

Finally, as in the case of the FKM imaging functional, it can be efficient to truncate the double sum in the KM imaging functional (3.18) over a limited offset range:

$$
\mathcal{I}^{\mathrm{KM}}\big(\boldsymbol{y}^S\big) = \sum_{\substack{j,l=1 \\ |\boldsymbol{x}_j - \boldsymbol{x}_l| \leq y_{\max}}}^{N} C_T\big(\tau(\boldsymbol{y}^S, \boldsymbol{x}_l) - \tau(\boldsymbol{y}^S, \boldsymbol{x}_j), \boldsymbol{x}_j, \boldsymbol{x}_l\big). \qquad (3.22)
$$

Indeed this truncation may be useful when the travel times are perturbed because of lack of knowledge of the background velocity or because the medium is cluttered. In this situation, the terms $C_T\big(\tau(\boldsymbol{y}^S, \boldsymbol{x}_l) - \tau(\boldsymbol{y}^S, \boldsymbol{x}_j), \boldsymbol{x}_j, \boldsymbol{x}_l\big)$ for large offset $|\boldsymbol{x}_j - \boldsymbol{x}_l|$ are not reliable and bring only noise contributions. By truncating the double sum, one removes these noisy contributions. The choice of the optimal $y_{\max}$ is a trade-off between noise reduction and loss of resolution.

3.4. Comparison with High-Frequency Inversion. The comparison of our imaging formula with the standard KM functional is not complete in that High-Frequency Inversion (HFI) formulas have been proposed and studied that improve the quality and resolution of the standard KM. In this section we follow the procedure first proposed by Beylkin [2] and subsequently developed by many authors (see [4] and references therein). The idea is once again to look at the inversion formula (3.3) and to identify the kernel $\hat{B}$ so that $\mathcal{I}(\boldsymbol{y}^S)$ is as close as possible to $K(\boldsymbol{y}^S)$ in the high-frequency regime. Writing the search point $\boldsymbol{y}^S = (x, z)$ and making the change of variables $(x_1, x_2) = (\xi + h/2, \xi - h/2)$ in the integral, the inversion formula (3.3) can be written as

$$
\mathcal{I}\big((x,z)\big) = \frac{1}{2\pi} \iint \hat{B}_{x,z,h}(\omega, \xi) e^{i\omega[\tau((\xi+h/2,0),(x,z)) - \tau((\xi-h/2,0),(x,z))]}
$$

$$
\times \hat{C}(\omega, \xi + h/2, \xi - h/2) d\omega \, d\xi \, dh. \qquad (3.23)
$$

Substituting the high-frequency approximation (3.2) of the cross correlation we obtain

$$\mathcal{I}((x,z)) = \frac{1}{2\pi} \iint \hat{B}_{x,z,h}(\omega,\xi) \frac{\hat{F}(\omega)}{|\omega|} K(x_s,z_s)$$
$$\times e^{i\omega[\tau((\xi+h/2,0),(x,z))-\tau((\xi-h/2,0),(x,z))]} e^{-i\omega[\tau((\xi+h/2,0),(x_s,z_s))-\tau((\xi-h/2,0),(x_s,z_s))]}$$
$$\times a\big((\xi+h/2,0),(x_s,z_s)\big) a\big((\xi-h/2,0),(x_s,z_s)\big) d\omega d\xi dx_s dz_s dh.$$

If we choose $\hat{B}_{x,z,h}(\omega,\xi) = 1$ then we obtain the standard KM functional (3.19). This functional is somewhat close to the function K, but it is possible to improve the quality of the inversion with a better choice for the kernel $\hat{B}_{x,z,h}(\omega,\xi)$. We anticipate that the integral in (x_s,z_s) is concentrated around (x,z), so we expand the phase and the amplitude terms into the Taylor series about the point $(x_s,z_s) = (x,z)$ and $h=0$ and we obtain:

$$\mathcal{I}((x,z)) = \frac{1}{2\pi} \iint \hat{B}_{x,z,h}(\omega,\xi) \frac{\hat{F}(\omega)}{|\omega|} K(x_s,z_s) a^2\big((\xi,0),(x,z)\big)$$
$$\times \exp\left(i\frac{\omega}{c_0} h \frac{z}{((x-\xi)^2+z^2)^{3/2}}[z(x_s-x)+(\xi-x)(z_s-z)]\right) d\omega d\xi dx_s dz_s dh.$$

We next make the change of variables $(\omega,\xi) \to (k_1,k_2)$ with

$$k_1 = \frac{\omega}{c_0} h \frac{z^2}{((x-\xi)^2+z^2)^{3/2}}, \qquad k_2 = \frac{\omega}{c_0} h \frac{z(\xi-x)}{((x-\xi)^2+z^2)^{3/2}},$$

whose Jacobian is

$$J_h(\omega,\xi) = \begin{vmatrix} \frac{\partial k_1}{\partial \omega} & \frac{\partial k_2}{\partial \omega} \\ \frac{\partial k_1}{\partial \xi} & \frac{\partial k_2}{\partial \xi} \end{vmatrix} = \frac{h^2|\omega|}{c_0^2} \frac{|z|^3}{((x-\xi)^2+z^2)^3}$$

and inverse function is

$$\omega_h(k_1,k_2) = \frac{c_0|z|}{h} \frac{(k_1^2+k_2^2)^{3/2}}{k_1^2} \mathrm{sgn}(k_1), \quad \xi_h(k_1,k_2) = x + z\frac{k_2}{k_1}.$$

By following Beylkin's idea we choose $\hat{B}_{x,z,h}(\omega,\xi) = \hat{B}_{x,z,h}^{\mathrm{HFI}}(\omega,\xi)$, where $\hat{B}_{x,z,h}^{\mathrm{HFI}}(\omega,\xi)$ is such that

$$\hat{B}_{x,z,h}^{\mathrm{HFI}}(\omega,\xi) \frac{a^2\big((\xi,0),(x,z)\big)}{|\omega|J_h(\omega,\xi)} = \frac{1}{2\pi},$$

or equivalently

$$\hat{B}_{x,z,h}^{\mathrm{HFI}}(\omega,\xi) = \frac{4h^2\omega^2}{c_0^3} \frac{|z|^3}{\big((x-\xi)^2+z^2\big)^{5/2}}. \tag{3.24}$$

With this choice the kernel is proportional to h^2. This means that it enhances the contributions of the cross correlations of observation points with large offsets (i.e., that are far from each other). This makes sense since the zero-offset cross correlations do not carry information in their phases because the differences of travel times are zero. This is fundamentally different from reflection seismology in which the sum of travel times appears and the zero-offset contributions of the impulse response matrix carries useful information [4].

With the choice (3.24) the HFI functional defined by

$$\mathcal{I}^{\mathrm{HFI}}\big((x,z)\big) = \iint \hat{B}_{x,z,h}^{\mathrm{HFI}}(\omega,\xi)e^{i\omega[\tau((\xi+h/2,0),(x,z))-\tau((\xi-h/2,0),(x,z))]}$$
$$\times \hat{C}(\omega,\xi+h/2,\xi-h/2)d\omega d\xi dh \quad (3.25)$$

has the following expression in the high-frequency regime

$$\mathcal{I}^{\mathrm{HFI}}\big((x,z)\big) = \frac{1}{(2\pi)^2}\iint \hat{F}\big(\omega_h(k_1,k_2)\big)K(x_s,z_s)e^{ik_1(x_s-x)+ik_2(z_s-z)}dk_1 dk_2 dx_s dz_s dh.$$

If $\hat{F}$ is constant, then the integrals over k_1 and k_2 produce Dirac distributions at $x_s = x$ and $z_s = z$ and we obtain that the HFI functional is proportional to the function K:

$$\mathcal{I}^{\mathrm{HFI}}\big((x,z)\big) \sim K(x,z).$$

The hypothesis that $\hat{F}$ is constant is reasonable in the context of reflection seismology, in which the sources are (more or less) known and broadband. That is partly why this procedure is very popular in this domain. Note also that the integral over the offset enhances the amplitude of the functional, but is not a crucial ingredient. The procedure would work with a limited number of offset values, in fact, it may also work well even though $\hat{F}$ is relatively strongly varying, see the numerical experiments below.

The hypothesis that $\hat{F}$ is constant is certainly not realistic in the context of noise sources. However, it is possible instead to integrate over many offsets, say with respect to an even function $\psi(h)$ whose support is in $[-h_{\max}, h_{\max}]$. In such a situation, we obtain after the change of variable $h \to \omega = \omega_h(k_1,k_2)$:

$$\mathcal{I}^{\mathrm{HFI}}\big((x,z)\big) = \frac{c_0|z|}{(2\pi)^2}\iint \frac{\hat{F}(\omega)}{\omega^2}K(x_s,z_s)\frac{(k_1^2+k_2^2)^{3/2}}{k_1^2}\mathrm{sgn}(k_1)\psi\Big(\frac{c_0|z|}{\omega}\frac{(k_1^2+k_2^2)^{3/2}}{k_1^2}\Big)$$
$$\times e^{ik_1(x_s-x)+ik_2(z_s-z)}dk_1 dk_2 dx_s dz_s d\omega.$$

We can see here that the HFI functional is not optimal in this context since the integration over k_1 and k_2 does not produce exact Dirac distributions anymore, but smoothed versions of them. The FKM functional may then be a better choice in the case when we can sum over many offsets.

3.5. Numerical simulations. In this section we carry out numerical simulations in an open two-dimensional homogeneous medium. The source distribution is modeled by a collection of point sources randomly distributed in a compactly supported domain. The point sources emit stationary random signals with Gaussian statistics and zero-mean. The power spectral density is $\hat{F}(\omega) = \omega^4 \exp(-\omega^2/100)$. The background velocity is one. Therefore the carrier frequency is $\omega_0 \simeq 14$ and the carrier wavelength is $\lambda_0 \simeq 0.45$. There are 100 sensors at the surface $z = 0$ separated by $\delta x = 0.125$ in the interval $x \in (-6.25, 6.25)$. This corresponds to a dense array for (almost) all frequencies in the bandwidth. There are 150 independent point sources randomly distributed in the three rectangles $[-1.5, -1] \times [-10.5, -9.5]$, $[-1, -0.5] \times [-8.5, -8]$, and $[-0.5, 0] \times [-10.5, -9.5]$. The simulations are carried out in the frequency domain with the explicit form (2.6) of the Green's function for the background medium and 256 frequencies regularly sampled from 0 to $2\pi \times 255 \times \delta t^{-1}$,
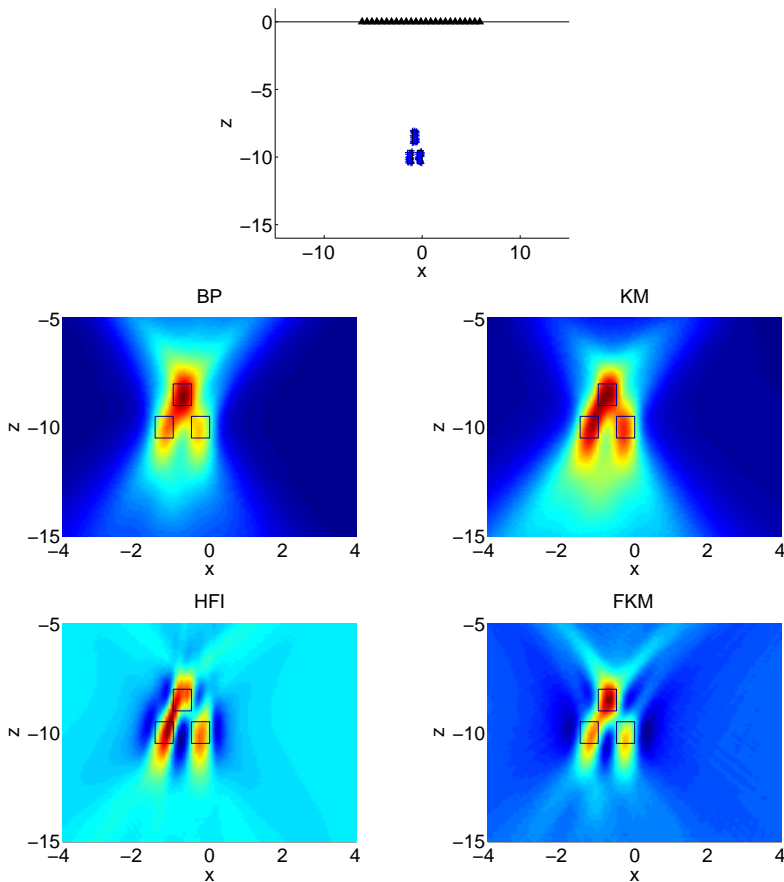
FIG. 3.1. *Imaging the sources. The numerical set-up is plotted in the top figure, where the triangles represent the sensors at the surface $z = 0$ and the independent point sources lie in the three rectangles in the subsurface. The images obtained with the different methods are plotted in the other figures (the BP function (3.16), the KM function (3.18), the HFI function (3.25), and the FKM function (3.15)).*

$\delta t = 0.125$. The reconstruction grid is a 100×100 uniform grid on the square $[-4, 4] \times [-15, -5]$. There is no need to introduce a cut-off parameter y_{max} here as the medium is homogeneous.

We compare the images obtained with the BP function (3.16), the KM function (3.18), the HFI function (3.25), and the FKM function (3.15) in Figure 3.1. We observe a resolution enhancement obtained with the FKM method as compared to the standard KM method or the BP method. These numerical simulations are in agreement with the theoretical predictions obtained in the high-frequency regime.

4. Imaging the medium. In this section we assume that the sensors are at the surface $z = 0$ and that the sources are in the subsurface below some depth $-z_0$. The medium is homogeneous in the half-space $z \in (-\infty, -z_0)$. The goal is to image the inhomogeneous region located in the section $z \in (-z_0, 0)$.

4.1. Born approximation. We model the scattering region as a perturbation $V(\boldsymbol{x})$ in the propagation speed as follows:

$$\frac{1}{c^2(\boldsymbol{x})} = \frac{1}{c_0^2} + V(\boldsymbol{x}), \tag{4.1}$$

where $V(\boldsymbol{x})$ is a function that has a compact support in the section $z \in (-z_0, 0)$. It is the function (or at least, its support) that we want to identify from the cross correlations of the signals recorded at the surface.

The solution of the wave equation with inhomogeneous speed $c(\boldsymbol{x})$ can be written as a sum

$$u(t, \boldsymbol{x}) = u_0(t, \boldsymbol{x}) + u_1(t, \boldsymbol{x}).$$

Here the direct field u_0 satisfies the homogeneous wave equation (2.1) with the background velocity c_0 and it is given by:

$$u_0(t, \boldsymbol{x}) = \iint G(t - s, \boldsymbol{x}, \boldsymbol{y}) n(s, \boldsymbol{y}) ds d\boldsymbol{y}, \tag{4.2}$$

where G is the homogeneous Green's function whose Fourier transform is (2.6). The scattered field u_1 is given by

$$u_1(t, \boldsymbol{x}) = -\iint G(t - s, \boldsymbol{x}, \boldsymbol{y}) V(\boldsymbol{y}) \frac{\partial^2 u}{\partial s^2}(s, \boldsymbol{y}) ds d\boldsymbol{y}.$$

This expression is exact. The Born approximation (or single-scattering approximation) consists in replacing u on the right side by the field u_0 [7]:

$$u_1(t, \boldsymbol{x}) \approx -\iint G(t - s, \boldsymbol{x}, \boldsymbol{y}) V(\boldsymbol{y}) \frac{\partial^2 u_0}{\partial s^2}(s, \boldsymbol{y}) ds d\boldsymbol{y}. \tag{4.3}$$

This approximation is valid if the scattered field u_1 is small compared to the incident field u_0, which corresponds to assuming that we are in the weakly scattering regime and that contributions of multiply-scattered waves can be neglected compared to the contributions of singly-scattered waves.

4.2. High-frequency analysis in the Born approximation. As in Subsection 3.1 we introduce the coherence time τ_c of the sources and the typical travel time τ_0. We also introduce the Wigner transform of the function V:

$$\hat{\Gamma}(\boldsymbol{x}; \boldsymbol{k}) = \int V\left(\boldsymbol{x} + \frac{\boldsymbol{y}}{2}\right) V\left(\boldsymbol{x} - \frac{\boldsymbol{y}}{2}\right) e^{-i\boldsymbol{k}\cdot\boldsymbol{y}} d\boldsymbol{y}$$

and denote by $1/\rho_c$ the typical width of $\boldsymbol{k} \to \hat{\Gamma}(\boldsymbol{x}; \boldsymbol{k})$. The length ρ_c is the correlation radius of the scattering region. We say that the scattering region is smooth if $\rho_c \gg c_0 \tau_c$ and that it is rough if $\rho_c \ll c_0 \tau_c$.

PROPOSITION 4.1. *We consider the high-frequency regime $\tau_c \ll \tau_0$.*

Case 1) If the scattering region is rough $\rho_c \ll c_0 \tau_c$, and if the sources are much deeper than the scattering region, then by denoting

$$\hat{\Gamma}_1(\boldsymbol{x}) = \hat{\Gamma}(\boldsymbol{x}; \boldsymbol{0}), \tag{4.4}$$

the function R defined by (3.4) has a contribution proportional to the Radon transform of $\hat{\Gamma}_1$:

$$R(s,\phi) \simeq r_0 \, \mathrm{RT}\big(K\big)(s,\phi) + r_1(K) \, \mathrm{RT}\big(\hat{\Gamma}_1\big)(s,\phi), \qquad (4.5)$$

where the Radon transform is defined by (3.6) and the constant $r_1(K)$ is

$$r_1(K) = \frac{c_0^2}{64\pi^2}\Big[\int |\omega|\hat{F}(\omega)d\omega\Big]\Big[\int \frac{K(\boldsymbol{x})}{|\boldsymbol{x}|}d\boldsymbol{x}\Big]. \qquad (4.6)$$

Case 2) If the scattering region is smooth $\rho_c \gg c_0\tau_c$ and if the local correlation is isotropic, i.e. $\hat{\Gamma}(\boldsymbol{x};\boldsymbol{k}) = \hat{\Gamma}(\boldsymbol{x};|\boldsymbol{k}|(1,0))$, then by denoting

$$\hat{\Gamma}_2(\boldsymbol{x}) = \int \hat{\Gamma}(\boldsymbol{x};\kappa(1,0))d\kappa,$$

the function R defined by (3.4) is of the form

$$R(s,\phi) \simeq r_0 \, \mathrm{RT}\big(K\big)(s,\phi) + r_2 \, \mathrm{RT}\big(K\big)(s,\phi) \, \mathrm{RT}\big(\hat{\Gamma}_2\big)(s,\phi), \qquad (4.7)$$

where the constant r_2 is

$$r_2 = \frac{c_0^3}{64\pi^2}\int \hat{F}(\omega)d\omega. \qquad (4.8)$$

It is very striking that the function R can be written in terms of the Radon transforms of K and $\hat{\Gamma}_j$. We can give the following interpretation of the different formulas.

In Case 1 the scattering region is rough so that scattering is isotropic. This induces an isotropization of the scattered field which forgets the directionality of the incident energy flux coming from the noise sources. That is why we find that the contributions of the scattered field to the function R is proportional to the Radon transform of $\hat{\Gamma}_1$ and depends on the source function K only through an averaged quantity. Note that $\hat{\Gamma}_1(\boldsymbol{x})$ characterizes the support of the scattering region. Since the support of the source region is well separated from the support of the scattering region, Eq. (4.5) shows that the inverse Radon transform of R in the region $z \in (-z_0, 0)$ will give the function $\boldsymbol{x} \to \hat{\Gamma}_1(\boldsymbol{x})$ up to a multiplicative constant.

In Case 2 the scattering region is smooth so that scattering is highly directional (in the forward direction). Therefore the scattered field keeps the memory of the incident energy flux coming from the noise sources. That is why we find that the contributions of the scattered field to the function R has the form of the product of the Radon transforms of the source function K and of the function $\hat{\Gamma}_2$. Moreover:
i) If the noise source distribution is (more or less) uniform, then the Radon transform of K is (more or less) constant and the inverse Radon transform of R in the region $z \in (-z_0, 0)$ gives the function $\boldsymbol{x} \to \hat{\Gamma}_2(\boldsymbol{x})$ up to a multiplicative constant.
ii) If the noise source distribution is not uniform and not known, then the inverse Radon transform of R in the region $z \in (-z_0, 0)$ gives

$$\mathrm{IRT}(R)\big(\boldsymbol{y}\big) = \frac{r_2}{4\pi^2}\int e^{i\boldsymbol{k}\cdot\boldsymbol{y}}\mathcal{K}_K\widehat{\hat{\Gamma}}_2(\boldsymbol{k})d\boldsymbol{k}, \quad \mathcal{K}_K\hat{\Gamma}_2(\boldsymbol{k}) = \int \hat{K}\Big(\kappa\frac{\boldsymbol{k}}{|\boldsymbol{k}|}\Big)\widehat{\hat{\Gamma}}_2\Big(\boldsymbol{k} - \kappa\frac{\boldsymbol{k}}{|\boldsymbol{k}|}\Big)d\kappa$$

This shows that we get a smeared version of $\widehat{\hat{\Gamma}}_2$, through the special convolution with $\hat{K}$, and of course the smearing is small when $\hat{K}$ has a small support.

iii) If the noise source distribution is not uniform but known (up to a multiplicative constant), then we can deconvolve the effects of the energy flux anisotropy in the sense that the inverse Radon transform of $R/\mathrm{RT}(K)$ in the region $z \in (-z_0, 0)$ will give the function $\boldsymbol{x} \to \hat{\Gamma}_2(\boldsymbol{x})$.

The hypothesis "the sources are much deeper than the scattering region" (case 1) or "the local correlation is isotropic" (case 2) allows us to get an explicit relation between the function R and the Radon transform of $\hat{\Gamma}_j$. If this does not hold, then we do not get the simple relation in terms of the multiplicative constant r_j but the relation still holds true qualitatively and the IRT of R still gives a good approximation of the support of the function $\hat{\Gamma}_j$. In more detail:

In Case 1, if the sources are not much deeper than the scattering region, then by denoting

$$\tilde{K}(\boldsymbol{x}) = \int \frac{K(\boldsymbol{x} - \boldsymbol{y})}{|\boldsymbol{y}|} d\boldsymbol{y}, \qquad \tilde{r}_1 = \frac{c_0^2}{64\pi^2} \int |\omega| \hat{F}(\omega) d\omega,$$

the function R defined by (3.4) is of the form

$$R(s, \phi) \simeq r_0 \, \mathrm{RT}(K)(s, \phi) + \tilde{r}_1 \, \mathrm{RT}(\tilde{K}\hat{\Gamma}_1)(s, \phi).$$

In Case 2, if the local correlation is not isotropic, then by denoting

$$\hat{\Gamma}_2^\phi(\boldsymbol{x}) = \int \hat{\Gamma}(\boldsymbol{x}; \kappa(\cos\phi, \sin\phi)) d\kappa,$$

the function R defined by (3.4) is of the form

$$R(s, \phi) \simeq r_0 \, \mathrm{RT}(K)(s, \phi) + r_2 \, \mathrm{RT}(K)(s, \phi) \, \mathrm{RT}(\hat{\Gamma}_2^\phi)(s, \phi). \tag{4.9}$$

Proof. Using the high-frequency approximation of the Green's function and the Born approximation, we obtain

$$C(\tau, \boldsymbol{x}_1, \boldsymbol{x}_2) = C_{dd}(\tau, \boldsymbol{x}_1, \boldsymbol{x}_2) + C_{ds}(\tau, \boldsymbol{x}_1, \boldsymbol{x}_2) + C_{sd}(\tau, \boldsymbol{x}_1, \boldsymbol{x}_2) + C_{ss}(\tau, \boldsymbol{x}_1, \boldsymbol{x}_2),$$

where C_{dd} is the cross correlation of the direct waves with themselves:

$$C_{dd}(\tau, \boldsymbol{x}_1, \boldsymbol{x}_2) = \frac{1}{2\pi} \iint a(\boldsymbol{y}_s, \boldsymbol{x}_1) a(\boldsymbol{y}_s, \boldsymbol{x}_2) K(\boldsymbol{y}_s)$$
$$\times e^{-i\omega[\tau + \tau(\boldsymbol{y}_s, \boldsymbol{x}_1) - \tau(\boldsymbol{y}_s, \boldsymbol{x}_2)]} \frac{\hat{F}(\omega)}{|\omega|} d\boldsymbol{y}_s d\omega,$$

C_{ds} and C_{sd} are the cross correlations of the direct and scattered waves:

$$C_{sd}(\tau, \boldsymbol{x}_1, \boldsymbol{x}_2) = \frac{1}{2\pi} \iint a(\boldsymbol{y}_s, \boldsymbol{y}_1) a(\boldsymbol{y}_1, \boldsymbol{x}_1) a(\boldsymbol{y}_s, \boldsymbol{x}_2) K(\boldsymbol{y}_s) V(\boldsymbol{y}_1)$$
$$\times e^{-i\omega[\tau + \tau(\boldsymbol{y}_s, \boldsymbol{y}_1) + \tau(\boldsymbol{y}_1, \boldsymbol{x}_1) - \tau(\boldsymbol{y}_s, \boldsymbol{x}_2)]} e^{-i\,\mathrm{sgn}(\omega)\pi/4} |\omega|^{1/2} \hat{F}(\omega) d\boldsymbol{y}_s d\boldsymbol{y}_1 d\omega,$$

$$C_{ds}(\tau, \boldsymbol{x}_1, \boldsymbol{x}_2) = \frac{1}{2\pi} \iint a(\boldsymbol{y}_s, \boldsymbol{x}_1) a(\boldsymbol{y}_s, \boldsymbol{y}_2) a(\boldsymbol{y}_2, \boldsymbol{x}_2) K(\boldsymbol{y}_s) V(\boldsymbol{y}_2)$$
$$\times e^{-i\omega[\tau + \tau(\boldsymbol{y}_s, \boldsymbol{x}_1) - \tau(\boldsymbol{y}_s, \boldsymbol{y}_2) - \tau(\boldsymbol{y}_2, \boldsymbol{x}_2)]} e^{i\,\mathrm{sgn}(\omega)\pi/4} |\omega|^{1/2} \hat{F}(\omega) d\boldsymbol{y}_s d\boldsymbol{y}_2 d\omega,$$

and C_{ss} are the cross correlations of the scattered waves with themselves:

$$C_{ss}(\tau, \boldsymbol{x}_1, \boldsymbol{x}_2) = \frac{1}{2\pi} \iint a(\boldsymbol{y}_s, \boldsymbol{y}_1) a(\boldsymbol{y}_1, \boldsymbol{x}_1) a(\boldsymbol{y}_s, \boldsymbol{y}_2) a(\boldsymbol{y}_2, \boldsymbol{x}_2) K(\boldsymbol{y}_s) V(\boldsymbol{y}_1) V(\boldsymbol{y}_2)$$

$$\times e^{-i\omega[\tau + \tau(\boldsymbol{y}_s, \boldsymbol{y}_1) + \tau(\boldsymbol{y}_1, \boldsymbol{x}_1) - \tau(\boldsymbol{y}_s, \boldsymbol{y}_2) - \tau(\boldsymbol{y}_2, \boldsymbol{x}_2)]} \omega^2 \hat{F}(\omega) d\boldsymbol{y}_s d\boldsymbol{y}_1 d\boldsymbol{y}_2 d\omega.$$

The contribution C_{dd} of the direct waves to the function R is known and is described in Proposition 3.1.

The evaluations of the contributions C_{ds} and C_{sd} can be carried out as the one for C_{ss}, as given below, and leads to the conclusion that the contributions of C_{ds} and C_{sd} to the IRT of the function R in (3.4) are negligible compared to the ones for C_{ss} in the high-frequency regime and in the region $z \in (-z_0, 0)$.

We now consider C_{ss} at two points $\boldsymbol{x}_1 = (x + y/2, 0)$ and $\boldsymbol{x}_2 = (x - y/2, 0)$ at the surface $z = 0$. We make the change of variables $\boldsymbol{y}_1 = \boldsymbol{y}_a + \boldsymbol{y}_b/2$ and $\boldsymbol{y}_2 = \boldsymbol{y}_a - \boldsymbol{y}_b/2$ in order to exhibit the Wigner transform $\hat{\Gamma}(\boldsymbol{x}, \boldsymbol{k})$ of V. We proceed as in the proof of Proposition 3.1 and we find that the contribution of C_{ss} to the function W_s defined by (3.8) is

$$W_s(x, \alpha) = \frac{c_0^2}{64\pi^2} \iint |\omega| \hat{F}(\omega) \frac{K(x_s, z_s)}{\sqrt{(z - z_s)^2 + (x_s - x + \frac{\alpha}{\sqrt{1-\alpha^2}} z)^2}}$$

$$\times \hat{\Gamma}\left(x - \frac{\alpha}{\sqrt{1-\alpha^2}} z, z; -\frac{\omega}{c_0}\beta_x, -\frac{\omega}{c_0}\beta_z\right) dx_s dz_s dz d\omega, \qquad (4.10)$$

where the last two arguments of $\hat{\Gamma}$ are:

$$\beta_x = \frac{x_s - x + \frac{\alpha}{\sqrt{1-\alpha^2}} z}{\sqrt{(z_s - z)^2 + (x_s - x + \frac{\alpha}{\sqrt{1-\alpha^2}} z)^2}} - \alpha,$$

$$\beta_z = \frac{z_s - z}{\sqrt{(z_s - z)^2 + (x_s - x + \frac{\alpha}{\sqrt{1-\alpha^2}} z)^2}} + \sqrt{1 - \alpha^2}.$$

Case 1: If we assume that the scattering region is rough and sources are much deeper than the scattering region, then the geometric term in (4.10) can be approximated by $1/\sqrt{z_s^2 + x_s^2}$ and the last two arguments of $\hat{\Gamma}$ can be replaced by 0, so that we get

$$W_s(x, \alpha) = r_1 \int \hat{\Gamma}\left(x - \frac{\alpha}{\sqrt{1-\alpha^2}} z, z; 0, 0\right) dz,$$

with r_1 given by (4.6). The contributions of the scattered field to the function R defined by (3.4) can be expressed as (3.10), which gives the desired result.

Case 2: If we assume that the scattering region is smooth then the arguments β_x and β_z are constrained to be small. This happens only if x_s is close to $x - z_s \alpha/\sqrt{1 - \alpha^2}$. Motivated by this remark we make the change of variable

$$x_s \to \kappa = \frac{\omega}{c_0} \frac{1 - \alpha^2}{|z_s - z|} \left[x_s - x + \frac{\alpha}{\sqrt{1-\alpha^2}} z_s\right],$$

and we obtain

$$W_s(x, \alpha) = \frac{c_0^3}{64\pi^2 \sqrt{1-\alpha^2}} \iint \hat{F}(\omega) K\left(x - \frac{\alpha}{\sqrt{1-\alpha^2}} z_s, z_s\right)$$

$$\times \left[\int \hat{\Gamma}\left(x - \frac{\alpha}{\sqrt{1-\alpha^2}} z, z; -\kappa\sqrt{1-\alpha^2}, -\kappa\alpha\right) d\kappa\right] dz_s dz d\omega.$$

If, additionally, $\hat{\Gamma}$ is isotropic, then the term in the square brackets becomes equal to $\hat{\Gamma}_2$ and the function W_s can be factorized as

$$W_s(x, \alpha) = \frac{r_2}{\sqrt{1-\alpha^2}} \Big[\int K\Big(x - \frac{\alpha}{\sqrt{1-\alpha^2}} z_s, z_s \Big) dz_s \Big] \Big[\int \hat{\Gamma}_2 \Big(x - \frac{\alpha}{\sqrt{1-\alpha^2}} z, z \Big) dz \Big].$$

The contributions of the scattered field to the function R defined by (3.4) can be expressed as in (3.10), which gives the desired result. $\square$

4.3. Imaging functional. Based on the high-frequency analysis of the previous subsection, we propose to image the medium from the empirical cross correlation matrix $(C_T(\tau, x_j, x_l))_{j,l=1,...,N}$ with the FKM functional

$$\mathcal{I}^{\text{FKM}}\big((x, z)\big) = \text{IRT}\big(R_T\big)(x, z), \tag{4.11}$$

where $z \in (-z_0, 0)$, $x \in \mathbb{R}$, and R_T is a quadrature approximation of the integral function

$$R_T(s, \phi) = \cos\phi \int_{-\infty}^{\infty} C_T\Big(\frac{\sin\phi}{c_0} y, \frac{s}{\cos\phi} + \frac{y}{2}, \frac{s}{\cos\phi} - \frac{y}{2} \Big) dy \tag{4.12}$$

on points corresponding to the sensor locations. This imaging functional is expected to provide a good image provided the illumination of the scattering region by the energy flux coming from the noise sources is isotropic enough. We will see in the numerical simulations of the next subsection that the method is in fact robust with respect to this point.

The standard KM method in this context was studied in [13]. In the terminology introduced in that paper, we deal with a backlight illumination configuration in which the region to be imaged is between the sources and the sensors. The analysis carried out in [13] then shows that the suitable KM imaging functional is once again $\mathcal{I}^{\text{KM}}$ defined by (3.18). The comparative analysis of the FKM and KM functionals goes along the same lines as in Subsection 3.3 and gives the same conclusion, proving the superiority of the FKM functional in terms of resolution enhancement in the high-frequency regime.

4.4. Numerical simulations. In the numerical simulations the background velocity is one and there are 100 sensors at the surface $z = 0$ separated by $\delta x = 0.125$ in the interval $x \in (-6.25, 6.25)$. We consider different sources/scatterers configurations. There are either 1 point source located at $(-20, -100)$ (Figure 4.1) or 4 point sources located at $(-20, -100)$, $(0, -100)$, $(20, -100)$, and $(40, -100)$ emitting independent noise signals (Figures 4.2-4.3). There are also 150 point scatterers with reflectivities 0.1 randomly distributed in the three rectangles $[-1.5, -1] \times [-10.5, -9.5]$, $[-1, -0.5] \times [-8.5, -8]$, and $[-0.5, 0] \times [-10.5, -9.5]$. Note that the scattering regions that we want to image in these simulations have the same spatial supports as the source regions that we imaged in the simulations of Subsection 3.5. This means that we try in both sets of simulations to image the same spatial region, but here this region is a scattering region illuminated by noise sources, while we tried to image the source region in Subsection 3.5. The power spectral density of the noise sources is $\hat{F}(\omega) = \omega^4 \exp(-\omega^2/40)$ in Figures 4.1-4.2, so that $|\omega|^3 \hat{F}(\omega)$ is quite similar to the spectral density used in the simulations of Subsection 3.5 and the spectrum of the noise signals scattered by the scattering region is similar to the one of the noise signals emitted by the sources in Subsection 3.5. The power spectral density of the
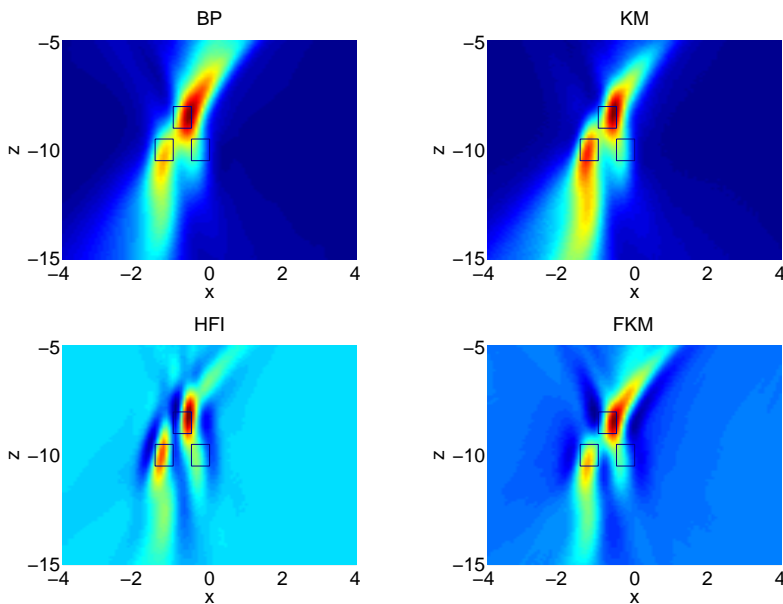
FIG. 4.1. *Imaging the medium when there is one point source located at $(-20, -100)$, three scattering regions (the three rectangles), and the power spectral density of the source is $\hat{F}(\omega) = \omega^4 \exp(-\omega^2/40)$.*

noise sources is $\hat{F}(\omega) = \omega^2(1 + \omega^2)^{-2} \exp(-\omega^2/400)$ in Figure 4.3 so that the source has relatively stronger low frequency in contents.

The situation in which there is only one point source (Figure 4.1) shows the improved resolution obtained with the FKM method compared to the BP and KM methods. One can see, however, that the direction of the energy flux coming from the source point has an impact on the image (the energy flux has approximately the direction of the vector $(1, 5)$ since the point source is located at $(-20, -100)$).

When there are four independent point sources (Figures 4.2-4.3), then the illumination of the scatterers has more directional diversity. Although the energy flux is still far from being isotropic, the directional diversity is sufficient to suppress the artefacts observed in Figure 4.1 in the case in which there is only one source. The FKM method produces an image which has a better resolution than the ones produced by BP, KM, or HFI. The improved resolution is especially striking in Figure 4.3.

5. Conclusions. In this paper we have set forth a promising passive imaging technique combining two well-known ideas: migration of cross correlation of noisy signals and inverse Radon transform. The theoretical high-frequency analysis and numerical simulations show the improved performance of the new imaging functional compared to the usual KM method. The KM method is almost equivalent to the new functional when the inverse filter is not used in the inverse Radon transform. Generalizations to three-dimensional media and non-homogeneous but slowly varying background using generalized Radon transforms, as well as a detailed resolution and signal-to-noise analysis, are in progress.
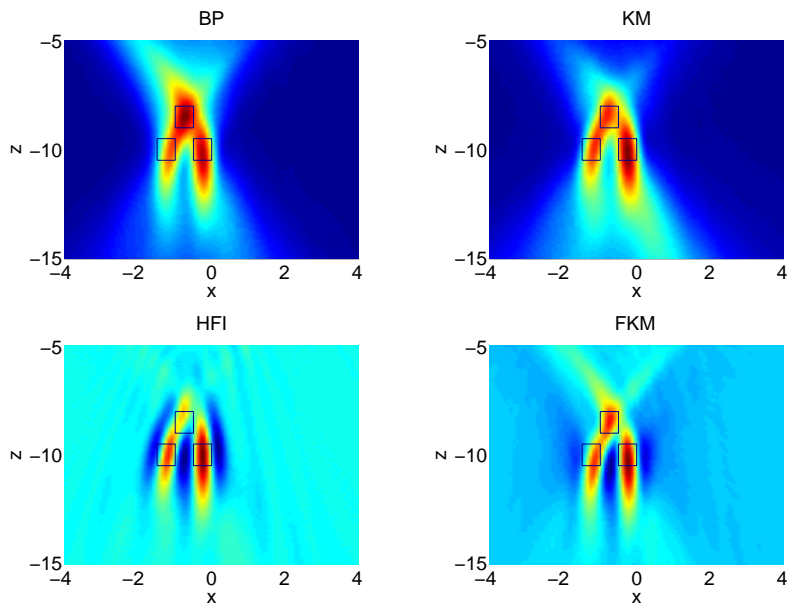
REFERENCES

FIG. 4.2. *Imaging the medium when there are four point sources located at* $(-20, -100)$, $(0, -100)$, $(20, -100)$, *and* $(40, -100)$, *three scattering regions (the three rectangles), and the power spectral density of the source is* $\hat{F}(\omega) = \omega^4 \exp(-\omega^2/40)$.
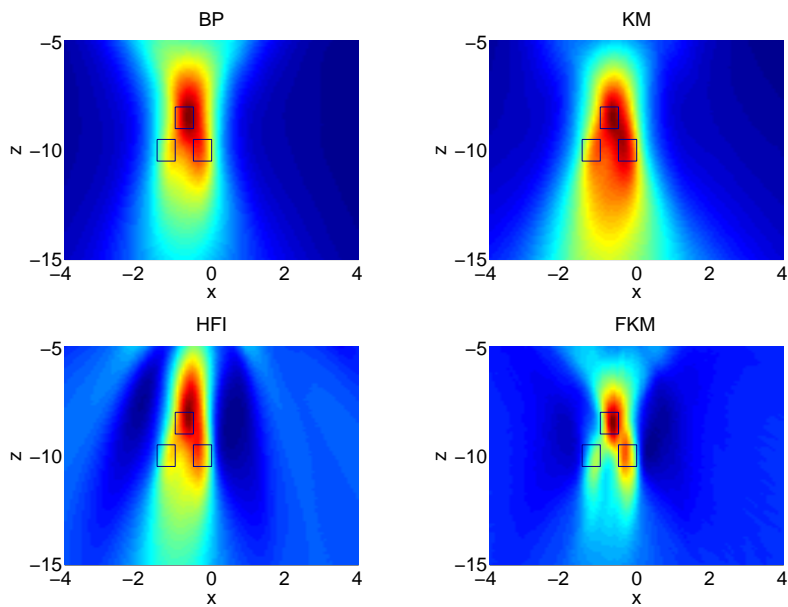

FIG. 4.3. *Imaging the medium when there are four point sources located at* $(-20, -100)$, $(0, -100)$, $(20, -100)$, *and* $(40, -100)$, *three scattering regions (the three rectangles), and the power spectral density of the source is* $\hat{F}(\omega) = \omega^2(1 + \omega^2)^{-2} \exp(-\omega^2/400)$.

[1] C. Bardos, J. Garnier, and G. Papanicolaou, Identification of Green's functions singularities by cross correlation of noisy signals, Inverse Problems, **24** (2008), 015011.

[2] G. Beylkin, Imaging of discontinuities in the inverse scattering problem by the inversion of a causal Radon transform, J. Math. Phys., **26** (1985), pp. 99-108.

[3] B. L. Biondi, *3D Seismic Imaging*, no. 14 in Investigations in Geophysics, Society of Exploration Geophysics, Tulsa, 2006.

[4] N. Bleistein, J. K. Cohen, and J. W. Stockwell Jr, *Mathematics of multidimensional seismic imaging, migration, and inversion*, Springer Verlag, New York, 2001.

[5] L. Borcea, G. Papanicolaou, and C. Tsogka, Interferometric array imaging in clutter, Inverse Problems, **21** (2005), pp. 1419-1460.

[6] L. Borcea, G. Papanicolaou, and C. Tsogka, Coherent interferometric imaging, Geophysics **71** (2006), pp. 1165-S1175.

[7] M. Born and E. Wolf, *Principles of optics*, Cambridge University Press, Cambridge, 1999.

[8] J. F. Claerbout, *Imaging the Earth's interior*, Blackwell Scientific Publications, Palo Alto, 1985.

[9] Y. Colin de Verdière, Semiclassical analysis and passive imaging, Nonlinearity, **22** (2009), pp. R45-R75.

[10] A. Curtis, P. Gerstoft, H. Sato, R. Snieder, and K. Wapenaar, Seismic interferometry - turning noise into signal, The Leading Edge, **25** (2006), pp. 1082-1092.

[11] M. de Hoop and K. Sølna, Estimating a Green's function from field-field correlations in a random medium, SIAM J. Appl. Math., **69** (2009), pp. 909-932.

[12] J. Garnier, Imaging in randomly layered media by cross-correlating noisy signals, SIAM Multiscale Model. Simul., **4** (2005), pp. 610-640.

[13] J. Garnier and G. Papanicolaou, Passive sensor imaging using cross correlations of noisy signals in a scattering medium, SIAM J. Imaging Sciences, **2** (2009), pp. 396-437.

[14] O. I. Lobkis and R. L. Weaver, On the emergence of the Green's function in the correlations of a diffuse field, J. Acoustic. Soc. Am., **110** (2001), pp. 3011-3017.

[15] F. Natterer and F. Wubbeling, *Mathematical methods in image reconstruction*, Society for Industrial and Applied Mathematics, Philadelphia, 2001.

[16] P. Roux and M. Fink, Green's function estimation using secondary sources in a shallow water environment, J. Acoust. Soc. Am., **113** (2003), pp. 1406-1416.

[17] K. G. Sabra, P. Gerstoft, P. Roux, and W. Kuperman, Surface wave tomography from microseisms in Southern California, Geophys. Res. Lett., **32** (2005), L14311.

[18] N. M. Shapiro, M. Campillo, L. Stehly, and M. H. Ritzwoller, High-resolution surface wave tomography from ambient noise, Science, **307** (2005), pp. 1615-1618.

[19] L. Stehly, M. Campillo, and N. M. Shapiro, A study of the seismic noise from its long-range correlation properties, Geophys. Res. Lett., **111** (2006), B10306.

[20] K. Wapenaar and J. Fokkema, Green's function representations for seismic interferometry, Geophysics, **71** (2006), pp. SI33-SI46.

[21] H. Yao, R. D. van der Hilst, and M. V. de Hoop, Surface-wave array tomography in SE Tibet from ambient seismic noise and two-station analysis I. Phase velocity maps, Geophysical Journal International, **166** (2006), pp. 732-744.